In situ nuclear magnetic resonance investigations of lithium ions in carbon electrode materials using a novel detector

2001 J. Phys.: Condens. Matter 13 8269

(http://iopscience.iop.org/0953-8984/13/36/304)

INSTITUTE OF PHYSICS PUBLISHING JOURNAL OF PHYSICS: CONDENSED MATTER

J. Phys.: Condens. Matter **13** (2001) 8269–8285 PII: S0953-8984(01)26838-6

In situ nuclear magnetic resonance investigations of lithium ions in carbon electrode materials using a novel detector

R E Gerald II[1], **J Sanchez, C S Johnson, R J Klingler and J W Rathke**

Chemical Technology Division, Argonne National Laboratory, Argonne, IL 60439, USA

E-mail: gerald@cmt.anl.gov (R E Gerald)

Received 13 July 2001
Published 23 August 2001
Online at stacks.iop.org/JPhysCM/13/8269

Abstract

The reversible electrochemical process (insertion/extraction) of lithium ions in graphitic carbon was monitored *in situ* for the first time by ^{7}Li nuclear magnetic resonance (NMR) spectroscopy using a novel NMR apparatus. The *compression coin cell battery imager* is a simple device that combines the functions of an electrochemical cell and an NMR detector. A series of ^{7}Li NMR spectra obtained for a blend of spherical and flaky disordered graphitic carbon particles revealed two distinct chemical shift signatures for the lithium ions that were inserted and extracted in the first electrochemical cycle. The lithium signal at ∼50 ppm is consistent with the interplane sites for lithium ions on the sixfold axis between two stacked aromatic carbon rings aligned in registry. The second predominant lithium signal at ∼12 ppm occurs in the chemical shift region reported for high-stage lithiated graphite and a dispersion of lithium-ion sites found in disordered carbon matrices. In addition, we observed chemical shift signatures similar to those assigned to Li-7 nuclei in lithium oxide, lithium carbonate, lithium alkyls, and lithium alkoxides that occur near 0 ppm and represent lithium nuclei that are irreversibly bound in the electrode/electrolyte interphase. An increase in intensity in the spectral region that is normally associated with irreversibly bound lithium was observed during the first discharge cycle, as anticipated. However, the same peaks in the spectrum unexpectedly diminished during the subsequent charge cycle, suggesting that the interphase between the carbon electrode and the electrolyte is built up over several cycles.

[1] Author to whom any correspondence should be addressed. Telephone: (630) 252-4214; fax: (630) 972-4458.

1. Introduction

1.1. Purpose

The purpose of this report is to demonstrate an *in situ* method for the investigation of electrochemical processes in electrode laminates by nuclear magnetic resonance (NMR) spectroscopy. We illustrate the method with an investigation of the electrochemical insertion and extraction of lithium ions in a graphitic carbon electrode. A diagram of the electrochemical process and the related terminology and conventions used in this study is shown as scheme 1. In brief, the electrochemical cell discharges spontaneously when lithium ions are reduced at the carbon cathode with the concomitant oxidation of metallic lithium at the anode. Electrons flow through an external circuit from the anode (+) to the cathode (−) to do work in an applied load. The electromotive force that drives the electrochemical process varies with the loading of lithium ions in the carbon electrode.

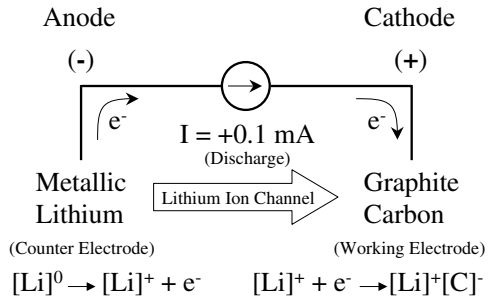

Scheme 1. The electrochemical cell indicating the nomenclature used in the text and the directions of the electronic and ionic currents.

A practical goal of this research is to develop a multinuclear NMR apparatus adaptable to flat laminated electrodes, and useful for *in situ* investigations of intercalation mechanisms and redox chemistries that occur at the surface and inside electrodes during electrochemical cycling. The initial focus of our efforts was to develop the *compression coin cell battery imager*, a novel apparatus useful for multinuclear NMR spectroscopy and imaging of flat coin cells. The detector apparatus and associated NMR techniques can be used *in situ* to quantitatively characterize:

(a) the spectroscopic signatures and distributions for the electrolyte components,
(b) the electrochemical reaction products formed at the surface and in the bulk electrode during electrochemical cycling,
(c) the microscopic mobility and distribution of lithium ions in the electrode lattice at different stages of lithiation,
(d) the reaction mechanism(s) for lithium-ion insertion/extraction encountered during the first and subsequent electrochemical cycles, and
(e) the electronic changes in the host carbon matrix.

We begin this paper with a discussion of the near-electrode imager because it is the predecessor of the present invention. We then describe the shortcomings of laminating the central rod of the near-electrode imager with novel anode and cathode materials that are of current interest in battery research. The difficult process of coating cylindrical rod electrodes motivated the development of the compression coin cell battery imager. This paper also discusses salient aspects of the toroid cavity NMR detector and related magnetic resonance

imaging methodologies relevant to the present work. In the results and discussion section, we illustrate the utility of the newly developed detector apparatus by applying it in the investigation of the cyclic insertion and extraction of lithium in a carbon mixture that is currently used in commercially available lithium-ion batteries by ^{7}Li NMR spectroscopy. The imaging capabilities of the NMR device used in this study can provide spatial discrimination of the electrochemical products at the two electrodes (e.g., formation of dendritic lithium at the cathode). However, a description of the imaging methodology using the compression coin cell battery imager is beyond the scope of this article.

1.2. Background

Wieckowski and co-workers have pioneered 'electrochemical NMR' in the solid state through ^{13}C and ^{195}Pt NMR investigations of several electrochemical systems (e.g., methanol on platinum black, NaCN and CH_3CN on a polycrystalline platinum electrode) [1–3]. In our previous *in situ* NMR investigations of electrochemical cells, we have focused on the mobility and distribution of ions in the electrolyte. For these investigations, we used the near-electrode imager device (see figure 1(a)), an electrochemical cell/NMR detector with cylindrical symmetry [4, 5]. In the near-electrode imager, a metal rod defines the axis of the cylindrical device, and functions simultaneously as the working electrode of the electrochemical cell and the central conductor of the toroid cavity NMR detector [6, 7]. A glass tube surrounds the central conductor and contains the sample. Within the glass tube a helical coil is positioned and used as a counter-electrode. The electrochemical cell assembly is contained in a toroid cavity as shown in figure 1(a). A potential applied between the central conductor and the outer cylinder produces a radial electric field that is used to displace ions dissolved in a supporting polymer matrix. With the near-electrode imager, the evolution of a salt concentration gradient was followed using ^{19}F NMR by imaging the concentration profile of the $[CF_3SO_3]^-$ (triflate) anion [8,9]. To extend the NMR investigations to novel electrode materials and the redox-active layer between the electrode and the electrolyte, several attempts were made to symmetrically

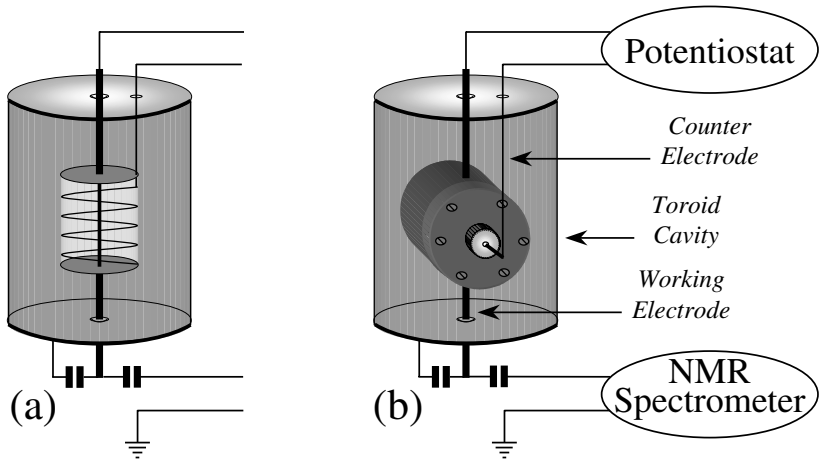

Figure 1. Schematic illustrations of two NMR detectors for *in situ* investigations of electrochemical cells. (a) The near-electrode imager has cylindrical symmetry and is suitable for investigations of oxidation/reduction reactions and the mobility of ions near the working electrode and in the bulk electrolyte. (b) The compression coin cell battery imager was designed to accommodate the geometry and dimensions of planar laminate electrodes used in commercial 2032-size coin cells.

coat the central working electrode (copper rod) with a uniform layer of different lithium intercalation compounds [10, 11]. Methods for coating the central conductor were developed, but mechanically robust coatings were difficult to fabricate. In addition, it was not a simple process to symmetrically compact a solid-film electrolyte and counter-electrode about the working electrode rod. However, standard methods exist for fabricating laminated electrodes on flat metal foils. Flat anode laminates, polymer electrolyte films, and cathode laminates can be easily stacked and compressed. Active electrode materials of current interest, including various carbon materials for negative electrodes and metal oxides for positive electrodes that intercalate lithium ions in lithium-ion batteries, are routinely prepared as flat laminates. Therefore, we developed a device, the compression coin cell battery imager for wide-line multinuclear NMR spectroscopy and imaging, that could take advantage of the ubiquitous flat laminate electrodes used in lithium-ion coin cells. In the present work we illustrate the utility of the new device with a ^{7}Li NMR spectroscopy study of the speciation of lithium in a carbon electrode.

The principal utility of ^{7}Li NMR spectroscopy is the insight it provides into the electronic environment surrounding Li^{+} ions in the intercalation process. Our first results using the flat imager were obtained *ex situ* on graphitic and sepiolite-templated carbon materials [12]. Our second results, also obtained *ex situ*, were on corannulene, a bowl-shaped aromatic hydrocarbon that has a greater capacity for lithium than graphite [13]. Both carbonaceous materials were completely lithiated (discharged to 0 V) in a conventional 2032 stainless steel coin cell. The lithiated carbon electrodes were then excised from the sealed cells and analysed by ^{7}Li NMR wide-line spectroscopy in the original coin cell battery imager. We learned from these experiments that we could analyse 10 mg of carbonaceous active anode material, detect the formation of dendrites at the surface of a carbon electrode, and form a hermetic battery seal that would last several days [13]. The *in situ* capability of the compression coin cell battery imager described here allows us to extend our previous experiments through the entire cycling process, so we can directly and unambiguously follow the various fractions of lithium ions in the different electronic environments. Thus, for example, we can: follow the potential profile for the formation of lithium clusters in the nanopores in hard carbons [14, 15]; address the degradation of reversible capacity with cycle number, which has been correlated with a high irreversible capacity in the first cycle and exfoliation of the carbon particles [16]; monitor the decomposition products of liquid and gel electrolytes at carbon and lithium electrodes during cycling [17–20].

2. Experimental procedure

2.1. Composition and fabrication of the carbon electrode

The carbon electrode investigated in this work was composed of a mixture of three powders: the active intercalation carbon; a flaky carbon material with a small grain size and good electrical conductivity; and a polymeric binder material. Yoshino *et al* empirically determined that a mixture of graphitic carbons with different particle sizes enhances the packing and electrical conductivity of the electrode [21]. The active intercalation carbon was a mesocarbon microbead material (MCMB-10) obtained from Osaka gas and made by heating coal tar to approximately 1300 K for several hours [21–23]. Heat treatments of coal tar above ∼1700 K cause excessive graphite crystal growth (graphitization); heat treatments below ∼1100 K result in inadequate electrical conductivity [21]. The flaky carbon (SFG-6) was purchased from Timcal (Westlake, OH). Poly(vinylidene fluoride) was used as the polymeric binder (Kynar®,

ATOFINA Chemicals). The carbons were mixed by weight, 65% MCMB-10 and 35% SFG-6. The mixture of carbons was then mixed by weight with the binder, 92% carbon mixture and 8% binder. The complete mixture was combined with *n*-methyl pyrollidone (NMP) to form a slurry and cast onto a flat 15 μm thick copper foil, which was used as the current collector, and mitred to a wet thickness of 100 μm using a doctor blade. The laminate was dried at room temperature and then flattened to a thickness of 66 μm by passing it through two counter-rotating steel rollers. A disc 15.9 mm (5/8″) in diameter was punched out of the laminate. The electrode disc contained 14.8 mg of the active lithium intercalation material (MCMB-10/SFG-6 graphite-blend carbon).

In order to describe the commercially obtained graphitic carbon that was used in our investigations we include estimates of a number of parameters for the structure and morphology of the carbon as determined from x-ray diffraction, BET isotherm, and density measurements obtained from the chemical literature for materials prepared by various methods [21–23]. Since the carbon used in our investigations was heat treated at approximately 1300 K, we surmise the following average material parameters [16, 21]: the average diameter of the carbon particles is 1–15 μm; the BET surface area is 5–10 $m^2\ g^{-1}$; the true density is 1.7–2.0 g cm^{-3}; the intersurface distance between the graphite planes, d_{002}, is 3.45–3.50 Å (3.71 Å for LiC_6); the dimensions of the graphitic carbon microstructure perpendicular to the graphite plane, $Lc_{(002)}$, and parallel to the graphite plane, $La_{(110)}$, are less than 40 Å each. In addition, for a quantitative description of the graphitic carbon structure, it is necessary to know the fraction of graphitic carbon that is hexagonal (2H) and rhombohedral (3R), and the degree to which the nominally parallel layers are shifted and rotated with respect to one another (turbostatic disorder) [16, 24–26]. These characteristics could not be inferred from the method of synthesis as described in references [21] and [16].

2.2. Electrochemical NMR detector assembly

The original near-electrode imager, and the compression coin cell battery imager designed to accommodate the component of a 2032-size coin cell are compared in figures 1(a) and 1(b), respectively [4, 27]. The coin cell press, NMR detector (also a current collector), and the internal components of an electrochemical cell are shown in the photograph in figure 2, and are arranged from left to right in the order in which they are stacked within the press assembly. The principal NMR detector element of the compression coin cell battery imager is a flat metal conductor in the shape of a circle. The flat (central) conductor simultaneously serves as the NMR detector element, and the current collector for the cathode electrode during the reductive intercalation process in the electrochemical cell. Significantly, the carbon cathode laminate is placed directly onto the flat circular detector in the compression coin cell battery imager instead of as a coating on the cylindrical wire detector used in the near-electrode imager. The flat detector element is connected at opposite ends to metal conductor rods that form part of an electromagnetic resonator circuit. The solid rods may be fabricated from an electrically conductive material (e.g., AlLi alloy) that provides an external magnetic resonance signature for use as a chemical marker and/or integration standard [28, 29]. A cylindrical metallic container (toroid cavity) is used to house the detector element and conductor rods. It provides a high-surface-area return path for electromagnetic RF currents that are conducted by the detector element, and serves as a shield to external sources of undesired alternating electromagnetic fields. Non-magnetic ceramic capacitors of fixed values (American Technical Ceramics Corporation, Jacksonville, FL) are soldered to the principal detector element for tuning to the desired nuclear resonance (Larmor) frequency and matching to the 50 Ω output impedance of the transceiver circuit.

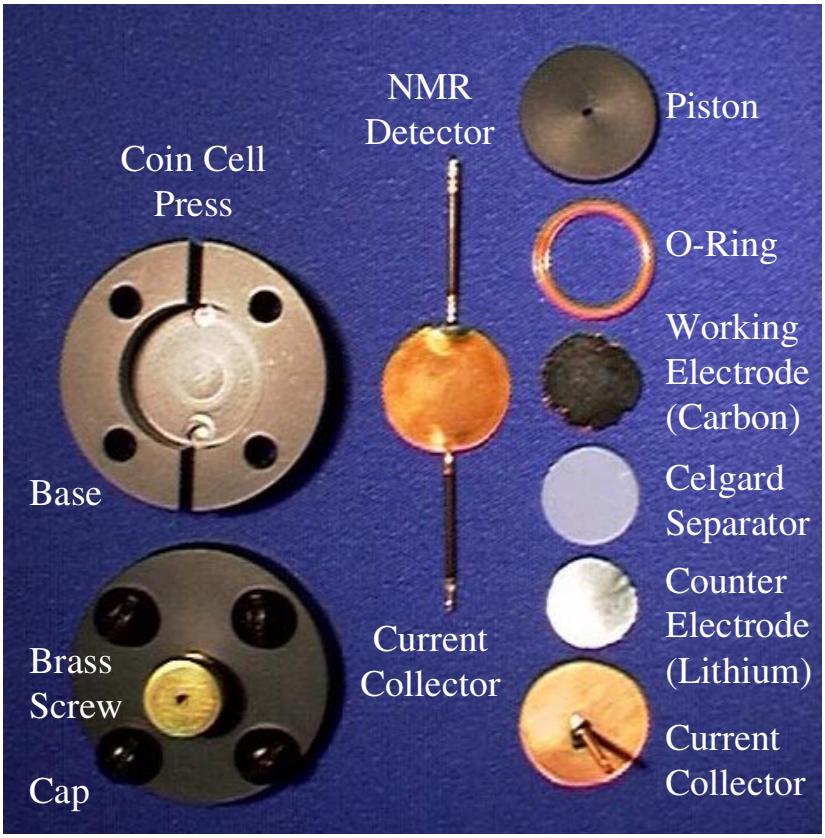

Figure 2. A photograph of the compression coin cell battery imager. The coin cell press holds the carbon sample to be analysed adjacent to the principal (NMR) detector element. The Teflon®-coated o-ring surrounds the electrodes of the coin cell and the corrosive electrolyte, and forms a hermetic seal at both copper current collector surfaces. The coin cell press is contained in a toroid cavity, which provides a return path for radio-frequency currents and shields out extraneous signals.

The cell is assembled in a similar manner to a standard 2032-size stainless steel button cell, in a dry room with a relative humidity of less than ∼1.53% (<400 ppm H_2O). The NMR detector is first placed in the cylindrical opening in the base of the plastic coin cell press. The base and cap of the coin cell press were made of Ultem® plastic (Comco Plastics, Incorporated). A Teflon® coated Viton® o-ring is placed on top of the detector to confine the cell components and the liquid electrolyte. Next, the carbon sample is placed in the cell press so that the copper foil back of the carbon laminate electrode makes electrical contact with the circular NMR detector element. A Celgard 2300 separator (Daramic, Incorporated) is placed above the carbon sample and saturated with a liquid electrolyte; it is permeable to the electrolyte, but is an electrical insulator that prevents an electrical short between the carbon laminate and lithium metal electrodes. A lithium metal disc is placed above the separator. A copper disc is then placed above the lithium disc and serves as a current collector. An electrically insulated wire is attached to the centre of the copper disc and directed perpendicular to the surface through a piston (Ultem®) and a brass thumbscrew, which is threaded through the cap of the press. The cap of the coin cell press is secured to the base by four black nylon screws. The brass

thumbscrew is used to apply pressure to the piston that in turn transmits a uniform pressure to the stacked components in the cell. The application of sufficient and uniform pressure ensures mechanical contact between the stacked components in the cell (anode, separator, cathode) with the result that the external potential is uniformly applied to the battery electrodes. In addition, the application of mechanical pressure to the piston simultaneously forms a gas-tight seal at the interfaces of the o-ring and both current collector discs.

2.3. Electrochemical NMR detector operation

The rate of energy exchange between the principal detector element and the NMR spin system is proportional to the strength of the RF magnetic field, B_1. The magnitude of the field inside the near-electrode imager is described analytically by $B_1 = A/r$, where A is a constant associated with the RF transmitter hardware and the efficiency of the detector, and r is the radial distance from the centre axis. The functional form of B_1 for the compression coin cell battery imager cannot be described analytically. As a consequence of the spatial B_1-inhomogeneity in both types of detector, there is no common nutation angle for the nuclei following an RF pulse. However, composite pulse sequences have been designed that reduce the effect of the inhomogeneous B_1-field on the NMR spectrum so that quantitative results can be obtained by the usual process of peak integration [30].

In order to analyse a sample (gas, liquid, or solid) held adjacent to the principal detector element, the compression coin cell battery imager is placed inside a static homogeneous magnetic field oriented perpendicular to the surface normal of the principal detector element. Transitions between adjacent nuclear magnetic energy levels are caused by the application of a pulse of RF current to the principal detector element. Following the RF pulse, electromagnetic RF signals emanate from the sample, are detected, and are recorded by a high-sampling-rate analogue-to-digital converter. A Fourier transform converts the time-domain signal (a free-induction decay) into the frequency-domain NMR spectrum. The NMR spectrum is then analysed for quantitative speciation (chemical composition) using different NMR-active nuclei in the sample (e.g., ^{7}Li, ^{19}F, ^{1}H, ^{13}C, ^{17}O). Between NMR experiments the battery is operated by connecting the potentiostat to a contact point on one rod that is connected to the principal detector element, and to another contact point on a wire lead connected to the current collector disc opposite the principal detector element. With this arrangement, alternating *in situ* electrochemical and NMR analyses can be made of the battery disc components and electrolyte.

The near-electrode imager and the compression coin cell battery imager can also be used for imaging experiments. The detectors generate a radio-frequency (RF) magnetic field gradient, ∇B_1, which can be employed for one-dimensional spatial imaging [6, 31]. Indeed, the well-defined B_1-field gradient within the near-electrode imager has been exploited for *in situ* imaging applications in electrochemical cells [8, 11]. In contrast, the compression coin cell battery imager does not have a simple analytical description for ∇B_1. The NMR imaging experiments are carried out in a homogeneous static B_0-field so that the chemical shift and coupling constant information for the sample can be recorded. The imaging methodology permits monitoring the spatial distribution of individual species in a wide range of materials. In the case of *in situ* investigations of coin cells, the imaging capability has been used to identify peaks in the NMR spectrum that derive from reaction products located at the working electrode (cathode). While the planar geometry of the compression coin cell imager easily accommodates flat laminate electrodes it deviates from the simple cylindrical geometry of the near-electrode imager, and the methodology for interpreting images obtained by the rotating-frame imaging (RFI) method

is complicated [32]. We anticipate that increasing the surface area of the NMR detector relative to the area occupied by the laminate electrode, and utilizing larger RF currents will simplify the mathematical formulation for processing images with micrometre resolution.

The design of the compression coin cell imager is a significant departure from the near-electrode imager because a flat circular disc replaces the central conductor (compare figure 1(a) and figure 2). This type of NMR imaging probe is distinguished by its simplicity of manufacture, ease of use, low cost, and high sensitivity. In contrast to conventional magnetic resonance imaging probes and techniques, the new probe conforms to the coin cell geometry, which maximizes the filling factor and the sensitivity for thin-film samples [33].

2.4. Electrochemical cycling

The electrochemical cycling experiments were conducted as follows. After the cell was assembled as described in section 2.2, the cell voltage was noted and an initial ^{7}Li NMR spectrum was recorded. The time period required to record a spectrum was 11.4 hours, and the recording was conducted overnight. The following day, the compression coin cell battery imager was disconnected from the NMR spectrometer console and cycled (intact) through the next cell transition using an EG&G model 273A potentiostat/galvanostat. The time period for the lithium insertion and extraction transitions varied from one to five hours each. Following each cell transition, the compression coin cell battery imager was disconnected from the potentiostat and reconnected to the NMR spectrometer console and a ^{7}Li NMR spectrum was recorded. During acquisition of the NMR spectrum, the electrochemical cell was at open-circuit potential. In the current implementation of the experiment, a ground loop between the NMR spectrometer console and the potentiostat provides an additional parallel current path that results in an error in the accumulated charge metered by the potentiostat. Therefore, we disconnect the compression coin cell imager from the potentiostat during the acquisition of the NMR data.

2.5. NMR spectrometer parameters

Wide-line ^{7}Li NMR spectra were recorded at room temperature (298 K) using a compression coin cell battery imager interfaced to a $^{\text{UNITY}}$INOVA-300WB spectrometer (Varian, Incorporated, Palo Alto, CA) at the following settings: spectrometer frequency, 116.592 080 MHz; spectral width, 100 kHz; radio-frequency pulse duration, 30 μs; data points recorded in quadrature, 8192; no zero-filling prior to Fourier transformation; recycle delay, 10.0 s; transients per spectrum, 4096. One-dimensional NMR spectra were processed with 20 Hz line broadening. A first-order phase correction of 95° was applied to produce a purely absorptive spectrum. The spin–lattice relaxation time constant for ^{7}Li nuclei in the graphitic carbon sample was not determined; however, from a series of previous experiments a recycle delay of 10 s was determined to be suitable for lithium nuclei in all electronic environments in lithium-ion cells except solvated Li^{+}, which required a recycle delay of more than 60 s. All ^{7}Li NMR chemical shifts were referenced to 0.0 ppm, the chemical shift for lithium in a 1.0 molar electrolyte solution of $LiPF_6$ in a 1:1 mixture by volume of ethylene carbonate and diethyl carbonate (Merck). An RF pulse length of 30 μs was chosen because it produced a purely absorptive signal for all the different lithium species in the cell. Quantitative information about the distribution of the different lithium signals is only achieved through a complete analysis of an image experiment and will not be described here.

3. Results and discussion

3.1. Electronic conductivity effects on NMR spectroscopy of electrodes

The spatial insertion of lithium ions from the electrolyte into graphite is driven by the reduction of lithium ions in the graphite working electrode and the concomitant oxidation of lithium atoms at the metallic lithium counter-electrode ($\Delta E > 0$ in scheme 1). The process requires that graphite conduct electrons. The electrical conductivity for graphite is about 15 orders of magnitude higher than for diamond [34]. The large difference in conductivity is due to the delocalized π-electrons in the two-dimensional graphite planes, compared to the exclusively localized covalent bonds in the three-dimensional structure of diamond. The conductivity of graphite is anisotropic with a bulk isotropic value of $7.273 \times 10^4\ \Omega^{-1}\ \mathrm{m}^{-1}$ (at 298 K). The conductivity in the basal planes is one order of magnitude greater than in the direction parallel to the surface normal (*c*-direction) [35]. The conductivity of graphite is more than two orders of magnitude lower than for metallic lithium ($\sim 10.6 \times 10^6\ \Omega^{-1}\ \mathrm{m}^{-1}$ at 298 K) [36]. The reductive intercalation of lithium in graphite to form LiC_6 enhances the conductivity to $\sim 2.0 \times 10^7\ \Omega^{-1}\ \mathrm{m}^{-1}$ (at 298 K), over two orders of magnitude higher than for bulk graphite alone, and within a factor of three of the conductivity of lithium [37, 38]. While electronic conductivity is necessary for the operation of the electrochemical cell it has two significant effects on the NMR spectroscopy experiments. First, the local phenomenon of electronic shielding for nuclei in diamagnetic materials is extended to include long-range effects from delocalized electrons. Second, the capacity of the electrode sample to conduct RF current may be a contributing factor of an anomalous enhancement that is observed in the NMR sensitivity.

3.2. Electronic shielding of lithium nuclei in electrical conductors

The electronic (chemical) shielding of a nucleus is a molecular property that results from the interaction of moving electronic charges with an external magnetic field. The interaction manifests itself in an induced magnetic field whose components are described in general by a non-symmetric second-rank tensor. In most diamagnetic materials the induced magnetic field opposes (shields) the external inducing magnetic field. Therefore, the net magnetic field experienced by the nucleus is smaller than the external magnetic field. The interaction is linear with field strength over the range of magnetic fields currently available for NMR spectroscopy and imaging. For electronic insulators, the chemical shift (a relative value for electronic shielding) of a nucleus is a local electronic property, influenced by the electronic structure within the dimensions of a few chemical bonds [39]. However, for electrical conductors, the electronic effects on a nucleus derive from an extended environment [40, 41]. The electrochemical process of lithium intercalation in graphite produces a corresponding and continuous change in the density of electronic states in the electrode material. The resultant variations in electronic conductivity can directly affect the local electronic environment of the lithium nucleus. Therefore, studies of ^{7}Li chemical shifts versus the level of lithium loading in graphite are necessary to define the number and types of local sites and the extended electronic environments for lithium in intercalant materials. The mobility of lithium in graphite can also affect the observed ^{7}Li chemical shift because the nucleus experiences an average electronic environment for all accessible sites. The intensive variables temperature and loading determine the population distribution of lithium among the different sites. Having experimental control of these variables will allow us to assign the observed resonance shifts to different local and extended lithium environments.

A large electronic shift, termed the Knight shift, results from delocalized electrons in the conduction bands of metals and semimetals [42, 43]. The ^{7}Li NMR Knight shift is a useful

electronic probe for the different lithium sites in electrode materials. The ^{7}Li Knight shift in LiC_6 is ∼50 ppm and is not as large as it is in lithium metal and lithium alloys (280–128 ppm) because the intercalate carbon material has a lower electronic conductivity [13, 28, 41, 44]. The chemical shifts of covalently bound lithium compounds have been measured, and fall in a limited range (∼±6 ppm) because of the small number of electrons surrounding the nucleus [45]. Therefore, one can determine from experimentally measured chemical shifts the different lithium species present in an electrochemical cell. In extended delocalized electronic systems, it is challenging to calculate Knight shifts. In metals, the density of states determines the Knight shift and this in turn depends on morphology and impurity atoms. Paramagnetic centres in the carbon matrix can cause large paramagnetic (deshielding) shifts. Our recent computational and experimental studies on curved carbon lattices have shown that lithium in corannulene and sepiolite-derived carbon have electronic multiplicities of 2 and 4 giving a paramagnetic shift to the ^{7}Li NMR resonance [12]. Exchange of lithium ions between carbon sites with different electronic environments can result in observed resonance shifts that should not be assigned to a single lithium (-ion) site. It is also possible that the lithium ions do not spatially exchange, but instead the environment around the lithium ions changes. That is, the lithium sites can undergo exchange through electron-transfer processes. This is probably the case in electrode systems where the extended electronic structure can transform with different degrees of lithium loading.

3.3. In situ ^{7}Li NMR spectrum of the active components of an electrochemical cell

The capability of the compression coin cell battery imager for *in situ* NMR spectroscopy is illustrated in figure 3. The ^{7}Li NMR spectrum can be used to readily identify the speciation of lithium in a Li-ion battery. The peak at ∼50 ppm in figure 3 has been assigned to the lithium ions intercalated between turbostatically disordered graphene planes as well as to extended graphite planes [46,47]. We have previously observed the ^{7}Li electric quadrupole satellite singularities in the powder pattern for lithium ions at the hexagonally symmetric sites in graphite using the original coin cell battery imager apparatus [12]. The peaks at 150 ppm and −50 ppm derive from the singularities in the powder pattern due to the $+3/2 \leftrightarrow +1/2$ and $-3/2 \leftrightarrow -1/2$ satellite transitions for Li-7 nuclei. Fortuitously, these singularities occur in regions of the spectrum that do not interfere with other peaks of interest, such as the region for inorganic and alkyl lithium near 0 ppm and the metallic lithium region near 275 ppm. For many carbon materials, these singularities are not observed. A range of electric quadrupole interactions deriving from different lithium sites that have similar Knight shift is one possibility for the observation of a broadened centre band and very diffuse or undetectable satellite singularities. Alternatively, a second reason would be an exchange mechanism where lithium ions move between different sites with the result that the features of a single static powder pattern are broadened. The lithium ions are mobile at 298 K and exchange between identical local sites with a residency time of 10^{-5} s [46]. The asymmetry parameter for the electric field gradient tensor is near zero. That is, the two principal components that are orthogonal to the largest principal component (V_{zz}) are nearly equal. This is consistent with the model of a hexagonally symmetric site for lithium. In the lithiated form of graphite, the graphite planes are in registry, with aromatic rings both above and below the lithium ion sites. Because the interaction between the magnetic dipole moment of the Li nuclei and the external static magnetic field is much larger than the interaction of the electric quadrupole moment with the electric field gradient at the nucleus (10^8 versus 10^1 kHz), the central line of the powder pattern is not shifted by the second-order electric quadrupole coupling interaction. The absolute value of the nuclear electric quadrupole ($|e^2qQ/h|$) interaction measured in the spectrum in figure 3

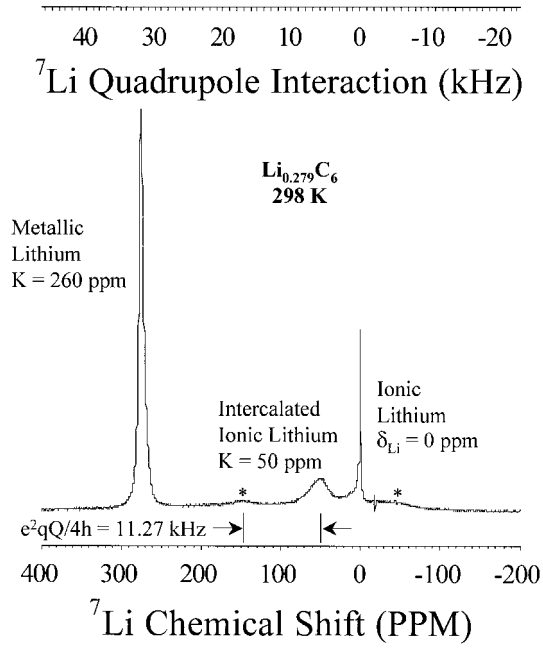

Figure 3. The *in situ* ^{7}Li NMR spectrum for all the active components in a lithium-ion electrochemical cell. The signature for metallic lithium at 275 ppm indicates the presence of the lithium metal counter-electrode. The sharp peak at 0 ppm derives from solvated lithium ions in the electrolyte. Bound lithium in the interphase between the electrolyte and the surfaces of the electrodes yields resonances in the range ±6 ppm. The peak at ∼50 ppm is centred between two broad satellite peaks. The group of three peaks represents the characteristic electric quadrupole powder pattern for ^{7}Li nuclei between two graphite planes.

is 45.1 kHz, which is similar to the value that we previously reported for a similar blend of graphite [12]. The value for the ambient-temperature coupling constant reported by Roth *et al* is 44.0 kHz [48] and that reported by Conard and Estrade is 48.0 kHz [46]. This interaction is temperature dependent over a large temperature range and increases from about 44 kHz at room temperature to 56 kHz at 4 K. No temperature dependence was observed for the Knight shift over the same temperature range [48]. Q_{cc} is also pressure dependent with pressure applied along the *c*-axis and has a coefficient of 1.5 kHz kbar^{-1} [38]. For large Q_{cc} only the central transition will be observed and an additional second-order shift will effect the position of the central transition frequency for very large Q_{cc}s. It is expected that lithium ions near edges will have large Q_{cc}s and, therefore, part of the observed chemical shift will be due to a Knight shift, which may be very weakly temperature dependent, and another part would be due to the electric Q_{cc}, which may be temperature dependent.

3.4. Electrochemical cycling of lithium in disordered graphitic carbon

The electrochemical lithium insertion curve (cell potential versus charge capacity) is shown in figure 4. The ^{7}Li NMR spectra that correspond to the break points are also shown. Note that little change was observed in the spectral region for lithium metal. Therefore, no dendritic lithium appears to have formed in the initial electrochemical cycles for this cell. The lithium loadings shown in table 1 were calculated by integrating the current versus time curve associated with the potential versus time plot. Dai *et al* suggested that their 17 ppm signal from a hard

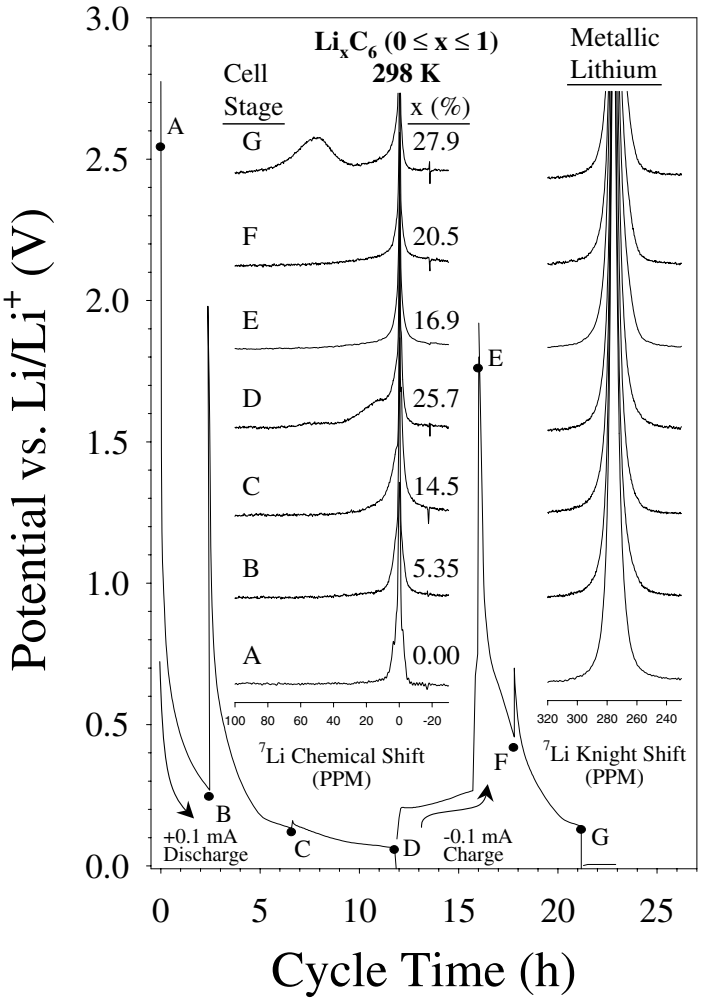

Figure 4. A composite graph illustrating the simultaneous acquisition of electrochemical voltage profiles (sequential plots of the electrode potential versus cycle time at constant current) and ^{7}Li NMR spectra for the electrochemical insertion (discharge) and extraction (charge) at constant current of lithium ions in a composite carbon working electrode. A ^{7}Li NMR spectrum was recorded at points labelled A–G on the voltage profile curve. The left inset represents the spectral region for intercalated lithium (∼50 ppm) and covalently bonded lithium (±6 ppm), and includes the lithium loading as a percentage of fully lithiated graphite (LiC_6). That is, x in Li_xC_6 ($0 < x < 1$) is indicated and expressed in %. The right inset represents the ^{7}Li resonance for metallic lithium, the counter-electrode.

carbon corresponds to lithium sites located in amorphous hydrogen-containing regions of the carbon [47]. With our approach, we make the more detailed assertion that the 17 ppm peak does not seem to emerge until below 0.160 V when already 17.41% lithium uptake has occurred (see transitions A–B–C in table 1). Lithium ions have high mobility at room temperature (site exchange rate of 100 000 s^{-1}) [46]. This means that if lithium ions exchange between different sites that have shifts that are different by about 10 000 Hz, a single resonance for the Li-7 nuclei will be observed. This may explain the variations in line shapes in the Li-7 NMR spectra as functions of temperature (near room temperature) reported by Gautier *et al* [49]. Exchange

Table 1. Cell transitions and corresponding cell voltages and capacities.

Cell transition[a]	Initial/final voltage between hold points (V)	Cycle time between hold points[b] (h)	Specific capacity for lithium insertion/extraction during transition[c] (mA h g^{-1})	Lithium loading: fraction of full specific capacity[d] (%)	Time at open-circuit voltage following cell transition[e] (h)
A → B	2.775/0.268	2.46 *ins.*	16.6 *ins.*	5.35	72
B → C	1.980/0.133	4.22 *ins.*	28.5 *ins.*	14.5	16
C → D	0.160/0.064	5.13 *ins.*	34.7 *ins.*	25.7	18
D → E	0.095/1.500	4.07 *ext.*	27.5 *ext.*	16.9	20
E → F	2.105/0.456	1.68 *ins.*	11.4 *ins.*	20.5	22
F → G	0.700/0.140	3.37 *ins.*	22.8 *ins.*	27.9	22

[a] Electrochemical staging. See figure 3.
[b] The time duration for galvanostatic discharging (lithium insertion, *ins.*) or charging (lithium extraction, *ext.*) of the cell to the hold point for acquisition of the NMR spectrum.
[c] Charge was metered galvanostatically at a rate of +0.1 mA during lithium insertion (*ins.*) and −0.1 mA during lithium extraction (*ext.*). A current density of 0.056 mA cm^{-2} was used, resulting in a full charge/discharge in 46 hours (rate: $\pm C/46$). The charge equivalent of 1.0 mA h is 3.6 coulomb (C). The calculations were based on an active carbon weight of 0.0148 g. Sample calculation: (0.1 mA × 2.46 h)/0.0148 g = 16.6 mA h g^{-1}.
[d] The specific theoretical capacity for LiC_6 is 372 mA h g^{-1} (1339.2 C g^{-1}). The table entries are equivalent to x (in per cent) for Li_xC_6 ($0 \leqslant x \leqslant 1$). The calculations were based on an average value for the actual reversible specific capacity of approximately 310 mA h g^{-1} for LiC_6. Sample calculation: ((16.6+28.5) mA h g^{-1}/310 mA h g^{-1}) × 100 = 14.5%. An actual irreversible specific capacity of approximately 10% of the actual reversible specific capacity (∼31 mA h g^{-1}) was not considered.
[e] Time spent by the cell at the hold points (at the open-circuit potential) for acquisition of the NMR spectra.

appears to take place between a site in a small graphene sheet and a site near a paramagnetic centre. The 12–17 ppm peak in our ^{7}Li NMR spectra may represent sites for lithium ions that are not located in regions with extended aromatic character, such as edge defect sites, where the Fermi level is not as full as it is for low-stage lithiated graphite (LiC_{12}–LiC_6) [50]. Wang *et al* observed a similar ^{7}Li NMR spectral component centred at 11–13 ppm (with $Q_{cc} = 39$ kHz), which they assigned to surface-bonded lithium atoms or lithium ions located at edge sites [51]. Alternatively, the 12–17 ppm peak that we observed may correspond to high-stage lithiated graphite as reported by Zaghib *et al* [52]. However, whereas Zaghib *et al* and Wang *et al* reported $Q_{cc} = 39$ kHz for a peak centred at 11–13 ppm, we did not observe a discernible quadrupole pattern for the 12–17 ppm peak in our spectrum. Several different mechanisms have been proposed for the electrochemical process of lithium intercalation in a wide variety of carbon materials [35, 47, 53–61].

3.5. Following the formation of the solid-electrolyte interphase (SEI)

Lithium uptake to 0.160 V resulted in the formation of lithium compounds (e.g., $LiCO_3$, LiO_2, LiR, LiOR) that are thought to comprise irreversible capacity of the electrode for lithium [16, 62]. The ^{7}Li NMR signatures for these compounds occur near 0 ppm [45]. This is borne out by the spectra shown in figure 5. However, the ^{7}Li NMR signals in this region show reversible behaviour in the first charge. Perhaps the inorganic lithium materials build up over the first few cycles with the result that the solid-electrolyte interphase (SEI) is dynamic and not fully formed in the first discharge. The SEI observed for carbon obtained from the pyrolysis of cotton cloth at 1300 K emerges during intercalation of lithium between potentials of 1.1 and 0.1 V [47]. We have found that the products from the electrochemical reduction of the electrolyte may not build up monotonically, but may appear to build up dynamically, over multiple cycles. It is possible that our data can be explained by dissolution of the SEI

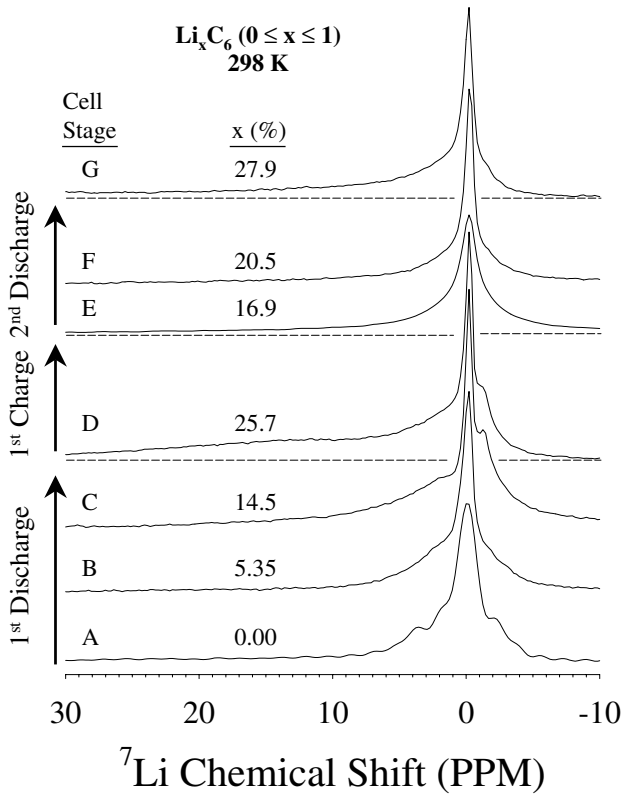

Figure 5. ^{7}Li NMR spectra for the expanded region near 0 ppm.

during a certain segment of the electrochemical cycle (e.g., during the initial portion of the discharge curve) or during the period of time for the NMR experiment when the cell is at open-circuit potential. This issue will be addressed more thoroughly in a modified experimental scheme that will allow continuous control of the cell voltage during the NMR experiment. The composition and the formation of the SEI has been investigated by several research groups, and is currently the focus of intensive research efforts [47, 60, 63–66].

4. Conclusions

We have developed the compression coin cell battery imager, a device that allows *in situ* NMR investigations of the electrodes in a button cell. In a single NMR spectrum it is possible to identify the coexistence of multiple lithium species, including lithium in the electrolyte, lithium in different intercalant environments, and inorganic lithium in the SEI. The lithium speciation can be followed continuously throughout multiple charge/discharge cycles. The compression coin cell battery imager allows the first true *in situ* observations to be made on lithium insertion electrodes during the actual charge/discharge process. Using this device we have found evidence for a transient response for graphite insertion electrodes that has not been described previously. Thus, during the initial cycle of lithium insertion we have observed a ^{7}Li NMR resonance feature, which grows in at 12–17 ppm. This feature is reversible. It decays during the subsequent lithium extraction process upon reversing the current. In addition, this

spectral feature is not observed on the second cycle. In contrast, we find on the second cycle only the formation of the standard ^{7}Li NMR signature for intercalated graphite near 50 ppm. Changes in the spectral region associated with the SEI were also found for the second cycle. We will continue these investigations to determine the sites that are responsible for this transient feature. Importantly, ^{7}Li NMR spectral features at 12–17 ppm are normally associated with irreversibly bound lithium. It is possible that the feature, which we found to be reversible on a short timescale, can transform into irreversible lithium over longer evolution times. In addition, we will investigate other carbon materials to determine how widespread these transient processes are with the ultimate long-range goal of better understanding the chemical pathway(s) for irreversible lithium formation in carbon insertion electrodes. Analogous experiments can be performed to analyse decomposition of the electrolyte using ^{1}H and ^{19}F NMR. Although challenging, it is also possible to monitor changes in the electronic structure of the graphite directly by ^{13}C NMR. In the future, it should be possible to spatially resolve the intercalated lithium in the electrode from the lithium species at the counter-electrode and in the electrolyte based on distance resolution using rotating-frame NMR imaging techniques. However, at this time the B_1-field dependence of the new flat coin cell geometry has not been rigorously defined mathematically and calibrated. This study was performed *in situ*; however, potentiostatic control was not maintained throughout the NMR experiments. An electronic modification to the interface between the potentiostat and the spectrometer will make it possible to maintain control of the potential throughout the NMR experiments. With additional refinements of the cell and method developments, it should be feasible to measure lithium diffusivity at different loadings of the carbon electrode, to monitor the distribution of lithium when the cell is allowed to relax at different stages in the electrochemical charge/discharge cycle, and to track the mass balance of lithium in its various forms in the anode, cathode, and electrolyte regions of the cell.

Acknowledgments

We are grateful to Dr Giselle Sandí (Chemistry Division, ANL) and Dr Daniel Colombo (Chemical Technology Division, ANL) for helpful discussions in this study. Dr Andrew Jansen kindly provided diagrams for a three-inch-diameter electrochemical cell that is widely used for testing large flat electrodes. His diagrams were helpful in the design of our NMR detector. We gratefully acknowledge the professional machinists that fabricated the compression coin cell battery imager: Chief Machinist W Brown and Instrumental Machinist R Maurisak. JS is grateful for a Community College Internship (CCI) Fellowship, a Commonwealth Edison Scholarship. JS is also grateful to NSF for an AMPS Scholarship. Support for this work was provided by the US Department of Energy, Division of Chemical Sciences, Office of Basic Energy Sciences, under Contract W-31-109-Eng-38.

References

[1] Wu J, Day J B, Franaszczuk K, Montez B, Oldfield E, Wieckowski A, Vuissoz P-A and Ansermet J-P 1997 *Faraday Trans.* **93** 1017
[2] Day J B, Vuissoz P-A, Oldfield E, Wieckowski A and Ansermet J-P 1996 *J. Am. Chem. Soc.* **118** 13 046
[3] Tong Y Y, Oldfield E and Wieckowski A 1998 *Anal. Chem.* **70** 518A
[4] Rathke J W, Klingler R J, Woelk K and Gerald R E II 2000 Near-electrode imager *US Patent Specification* 6046592, issued 4 April
[5] Rathke J W, Klingler R J, Gerald R E II, Kramarz K W and Woelk K 1997 *Prog. Nucl. Magn. Reson. Spectrosc.* **30** 209
[6] Woelk K, Rathke J W and Klingler R J 1994 *J. Magn. Reson.* A **109** 137

[7] Woelk K, Rathke J W and Klingler R J 1996 Nuclear resonance tomography with a toroid cavity detector *US Patent Specification* 5574370, issued 12 November
[8] Gerald R E II, Klingler R J, Rathke J W, Sandí G and Woelk K 1998 *Spatially Resolved Magnetic Resonance* ed P Blümler, B Blümich, R Botto and E Fukushima (New York: Wiley) ch 9, p 111
[9] Woelk K, Gerald R E II, Klingler R J and Rathke J W 1996 *J. Magn. Reson.* A **121** 74
[10] Sandí G, Gerald R E II, Scanlon L G, Carrado K A and Winans R 1998 *Materials for Electrochemical Energy Storage and Conversion II: Batteries, Capacitors and Fuel Cells; MRS Symp. Proc.* **496** 95
[11] Sandí G, Gerald R E II, Klingler R J, Rathke J W, Carrado K A and Winans R E 1999 *Proc. on Lithium Batteries* vol 98, ed S Surampudi and R Marsh (Pennington, NJ: Electrochemical Society) p 400
[12] Sandí G, Gerald R E II, Scanlon L G, Johnson C S, Klingler R J and Rathke J W 2000 *J. New Mater. Electrochem. Syst.* **3** 13
[13] Gerald R E II, Klingler R J, Sandí G, Johnson C, Scanlon L and Rathke J W 2000 *J. Power Sources* **89** 237
[14] Sato K, Noguchi M, Demachi A, Oki N and Endo M 1994 *Science* **264** 556
[15] Satoh A, Takami N, Ohsaki T, Oguchi M and Sasaki H 1998 *Denki Kagaku* **66** 1260
[16] Dahn J R, Sleigh A K, Shi Hang, Way B M, Weydanz W J, Reimers J N, Zhong Q and von Sacken U 1994 *Lithium Batteries: New Materials, Developments and Perspectives (Industrial Chemistry Library vol 5)* ed C Pistoia, p 1
[17] Dey A N and Sullivan B P 1970 *J. Electrochem. Soc.* **117** 222
[18] Kim D-W 1998 *J. Power Sources* **76** 175
[19] Scarr R F 1970 *J. Electrochem. Soc.* **117** 295
[20] Morigaki K and Ohta A 1998 *J. Power Sources* **76** 159
[21] Yoshino A, Sanechika K and Nakajima T 1987 *US Patent Specification* 4668595
[22] Mabuchi A, Tokumitsu K, Fujimoto H and Kasuh T 1995 *J. Electrochem. Soc.* **142** 1041
[23] Tatsumi K, Akai T, Imamura T, Zaghib K, Iwashita N, Higuchi S and Sawada Y 1996 *J. Electrochem. Soc.* **143** 1923
[24] Hérold A 1979 *Intercalated Layered Materials* vol 6, ed F Lévy, p 323
[25] Guerard D and Herold A 1975 *Carbon* **13** 337
[26] Holzwarth N A W and Rabii S 1977 *Mater. Sci. Eng.* **31** 195
[27] Gerald R E II, Klingler R J and Rathke J W 2000 Nuclear magnetic resonance imaging apparatus *US Patent Specification* DOE Case No S-95768, filed 3 August
[28] Gerald R E II, Nuñez L, Klingler R J and Rathke J W 1999 *Chemist* **76** 45
[29] Skibbe U and Neue G 1990 *Colloids Surf.* **45** 235
[30] Woelk K and Rathke J W 1995 *J. Magn. Reson.* A **115** 106
[31] Hoult D I 1979 *J. Magn. Reson.* **33** 183
[32] Woelk K, Zwank B L J, Trautner P, Lehnhof E, Bargon J, Klingler R J, Gerald R E II and Rathke J W 2000 *J. Magn. Reson.* A **145** 276
[33] Freeman R 1997 *A Handbook of Nuclear Magnetic Resonance* 2nd edn, p 248
[34] Emsley J 1991 *The Elements* 2nd edn (Oxford: Oxford University Press)
[35] Dresselhaus M S and Dresselhaus G 1981 *Adv. Phys.* **30** 139
[36] Lide D R (ed) 1999 *CRC Handbook of Chemistry and Physics* 80th edn (Boca Raton, FL: Chemical Rubber Company Press)
[37] Basu S, Zeller C, Flanders P J, Fuerst C D, Johnson W D and Fischer J E 1979 *Mater. Sci. Eng.* **38** 275
[38] Marinos C, Plesko S, Jonas J, Conard J and Guerard D 1983 *Solid State Commun.* **47** 645
[39] Tossell J A (ed) 1993 *Nuclear Magnetic Shieldings and Molecular Structure: Proc. NATO Advanced Research Workshop on the Calculation of NMR Shielding Constants and Their Use in the Determination of the Geometric and Electronic Structures of Molecules and Solids (College Park, MD, 20–24 July 1992)* (Dordrecht: Kluwer Academic)
[40] Abragam A 1961 *The Principles of Nuclear Magnetism* (Oxford: Clarendon)
[41] Carter G C, Bennett L H and Kahan P J 1977 *Metallic Shifts in NMR* part I (Elmsford, NY: Pergamon)
[42] Knight W D 1949 *Phys. Rev.* **76** 1259
[43] Winter J 1971 *Magnetic Resonance in Metals* (Oxford: Clarendon)
[44] Fischer J E 1979 *Intercalated Layered Materials* vol 6, ed F Lévy, p 481
[45] Akitt J W 1987 *Multinuclear NMR* ed J Mason, p 192
[46] Conard J and Estrade H 1977 *Mater. Sci. Eng.* **31** 173
[47] Dai Y, Wang Y, Eshkenazi V, Peled E and Greenbaum S G 1998 *J. Electrochem. Soc.* **145** 1179
[48] Roth G, Lüders K, Pfluger P and Güntherodt H-J 1981 *Solid State Commun.* **39** 423
[49] Gautier S, Leroux F, Frackowiak E, Faugére A M, Rouzaud J-N and Béguin F 2001 *J. Phys. Chem.* at press
[50] Holzwarth N A W, Rabii S and Girifalco L A 1978 *Phys. Rev.* B **13** 5190

[51] Wang Y, Yufit V, Guo X, Peled E and Greenbaum S 2001 *J. Power Sources* **94** 230
[52] Zaghib K, Tatsumi K, Sawada Y, Higuchi S, Abe H and Ohsaki T 1999 *J. Electrochem. Soc.* **146** 2784
[53] Acrivos J V 1979 *Intercalated Layered Materials* vol 6, ed F Lévy p 33
[54] Safran S A 1980 *Synth. Met.* **2** 1
[55] Dahn J R, Zheng T, Liu Y and Xue J S 1995 *Science* **270** 590
[56] Xue J S and Dahn J R 1995 *J. Electrochem. Soc.* **142** 3668
[57] Papanek P, Radosavljevic M and Fischer J E 1996 *Chem. Mater.* **8** 1519
[58] Zhou P, Papanek P, Bindra C, Lee R and Fischer J E 1997 *J. Power Sources* **68** 296
[59] Alcántara R, Fernández Madrigal F J, Lavela P, Tirado J L, Jiménez Mateos J M, Stoyanova R and Zhecheva E 1999 *Chem. Mater.* **11** 52
[60] Guérin K, Ménétrier M, Février-Bouvier A, Flandrois S, Simon B and Biensan P 2000 *Solid State Ion.* **127** 187
[61] Kim Y-O and Park S-M 2001 *J. Electrochem. Soc.* **148** A194
[62] Peled E 1979 *J. Electrochem. Soc.* **126** 2047
[63] Mori Y, Iriyama T, Hashimoto T, Yamazaki S, Kawakami F, Shiroki H and Yamabe T 1995 *J. Power Sources* **56** 205
[64] Zhou P, Papanek P, Lee R and Fischer J E 1997 *J. Electrochem. Soc.* **144** 1744
[65] Panitz J-C, Joho F and Novák P 1999 *Appl. Spectrosc.* **53** 1188
[66] Wang Y, Guo X, Greenbaum S, Liu J and Amine K 2001 *Electrochem. Solid State Lett.* **4** A68